

Recharged Catalyst with Memristive Nitrogen Reduction Activity through Learning Networks of Spiking Neurons

Gang Zhou, Tinghui Li, Rong Huang, Peifang Wang,* Bin Hu, Hao Li, Lizhe Liu,* and Yan Sun*



Cite This: *J. Am. Chem. Soc.* 2021, 143, 5378–5385



Read Online

ACCESS |



Metrics & More

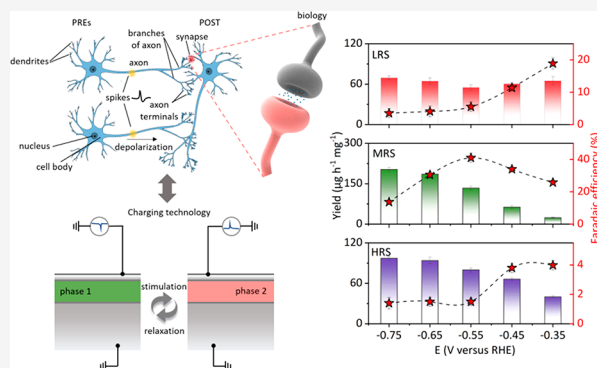


Article Recommendations



Supporting Information

ABSTRACT: Electrocatalysis from N_2 to NH_3 has been increasingly studied because it provides an environmentally friendly avenue to take the place of the current Haber–Bosch method. Unfortunately, the conversion of N_2 to NH_3 is far below the necessary level for implementation at a large scale. Inspired by signal memory in a spiking neural network, we developed rechargeable catalyst technology to activate and remember the optimal catalytic activity using manageable electrical stimulation. Herein, we designed double-faced $FeReS_3$ Janus layers that mimic a multiple-neuron network consisting of resistive switching synapses, enabling a series of intriguing multiphase transitions to activate undiscovered catalytic activity; the activation energy barrier is clearly reduced via an active site conversion between two nonequivalent surfaces. Electrical field-stimulated $FeReS_3$ demonstrates a Faradaic efficiency of 43% and the highest rate of $203 \mu g h^{-1} mg^{-1}$ toward NH_3 synthesis. Moreover, this rechargeable catalyst displays unprecedented catalytic performance that persists for up to 216 h and can be repeatedly activated through a simple charging operation.



INTRODUCTION

The electrochemical nitrogen reduction reaction (NRR) has been increasingly studied in relation to the development of crop fertilizers and the production of sustainable energy carriers in the hydrogen economy.^{1–4} Compared with the dominant Haber–Bosch method, electrochemical NRR technology can hydrogenate nitrogen as well as protons and electrons at room temperature and pressure.^{5,6} Substantial efforts have been invested in developing heterogeneous electrocatalysts to improve NRR activities and have mainly focused on enhancing their catalytic performances by tailoring nanostructure morphology, decreasing their thickness, creating vacancies or defects, doping or alloying, and crystal-phase engineering.^{7–11} However, most catalysts display a lower overpotential for the hydrogen evolution reaction (HER)^{12,13} than for the NRR and exhibit limited selectivity and activity for the NRR because of the critical challenge of overcoming the competitive HER.^{14–21} Therefore, the energy conversion efficiency and ammonia yield remain below those necessary for catalyst implementation at scale.

It is widely recognized that an excellent catalyst must present good NRR activity (a lower activation energy for the $N\equiv N$ triplet bond),²² a large Gibbs free energy for the HER (limiting H_2 generation),²³ a large superficial area (exposing more active sites)²⁴ and a low resistance for carrier transfer.²⁵ Basically, N_2 reduction efficiency can be enhanced by adjusting the intrinsic physical properties, such as structural transitions, of the material. However, it is very difficult to obtain various phase

structures through conventional synthesis strategies, especially for some particular phases with undiscovered NRR activity. Currently, a large challenge in phase-related catalysts is how to find undiscovered phases with outstanding catalytic performance and how to maintain them for long-term application. Unlike traditional microstructural strategies, this work concentrates on an easy and practical solution of improving NRR performance via electrical field stimulation, which is inspired by learning networks of spiking neuron devices,^{26–29} such as phase-related structure memory. These bionic designs involve dual-terminal semiconductor devices, which makes their physical properties (structural status) sensitive to external stimuli, such as a plasticity operation in biological synapses.^{30,31} If a series of phase transitions is realized and memorized via the learning work principle of a network of spiking neuron devices, particular phases with intriguing reaction kinetics can be discovered to boost NRR performance.

Thus, we propose a design strategy that mimics a biological neural subsystem, namely, an efficient electrical field stimulation system to drive the structural transition from a

Received: November 30, 2020

Published: March 31, 2021



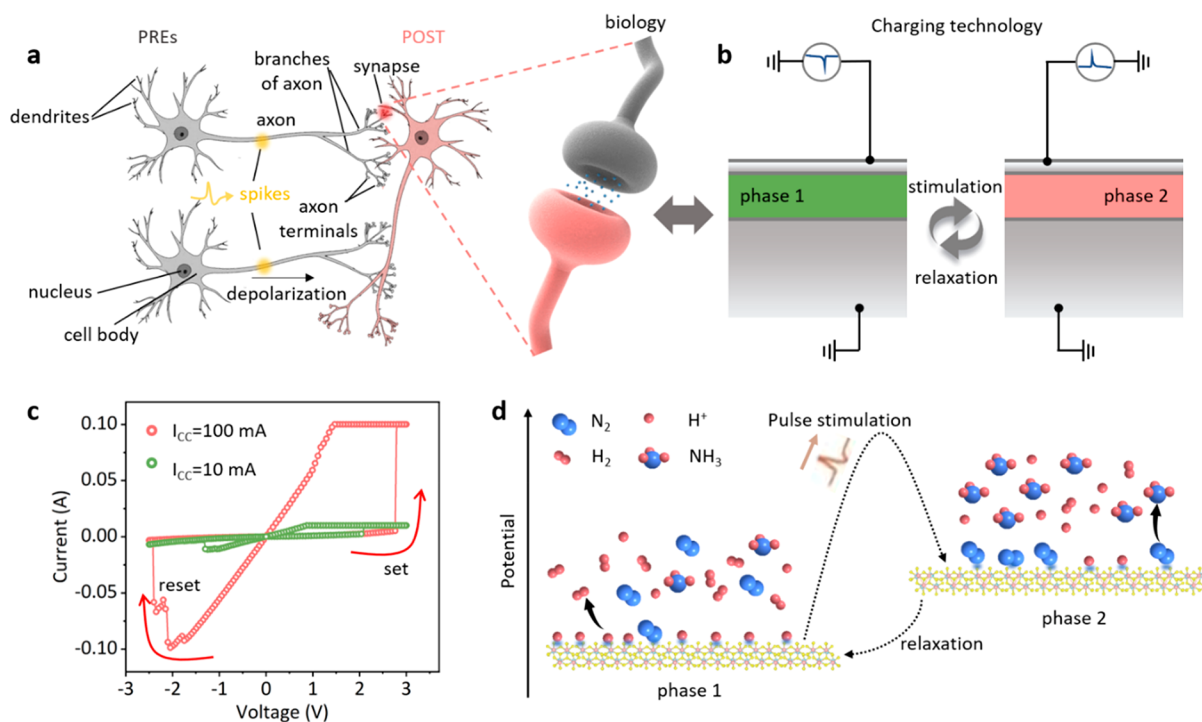


Figure 1. (a) Schematic showing the working principle of a neural subsystem. (b) PCM device designed to imitate the function of biological synapses. (c) Current–voltage (I – V) response of a PCM device. The phase transition can be regulated by varying I_{CC} . (d) Reaction activity of the phase-related catalyst before (left) and after (right) electrical stimulation.

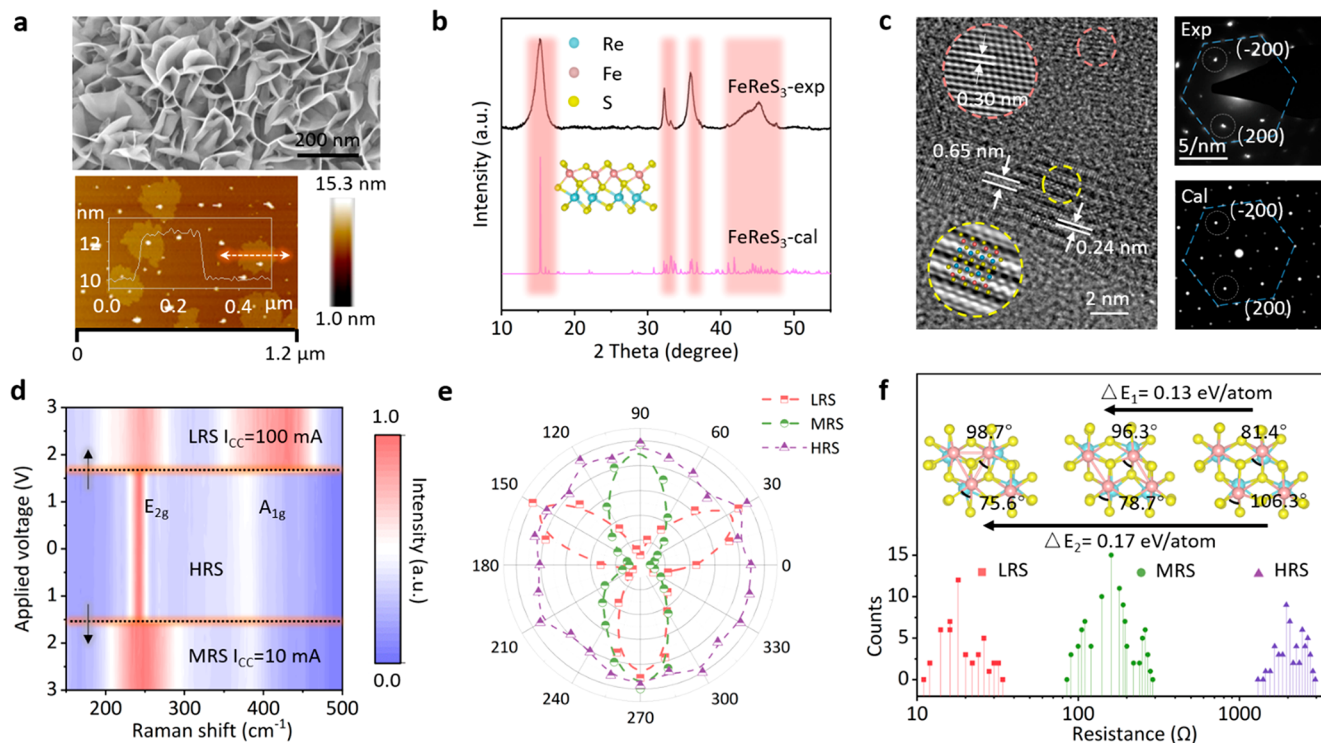


Figure 2. (a) SEM image (top) and AFM topographical image (bottom) of the FeReS_3 nanosheets. The bottom inset shows the height profile of the FeReS_3 nanosheet. (b) XRD patterns of the FeReS_3 samples (inset: a side view of the unit cell). (c) HR-TEM and SAED images of the FeReS_3 nanosheets. (d) Raman scattering map representing the broadening of the Raman mode and intensity under different I_{CC} conditions. (e) Polarization characteristics of the E_{2g} mode in the LRS, MRS, and HRS. (f) HRS/MRS/LRS resistance distribution of the FeReS_3 nanosheets (bottom) and their corresponding atomic configurations (top).

traditional phase to a particular structure with high catalytic activity. In a basic biological neural system (Figure 1a), a

postsynaptic neuron (POST) is linked by two presynaptic neurons (PREs) through synapses from POST dendrites to

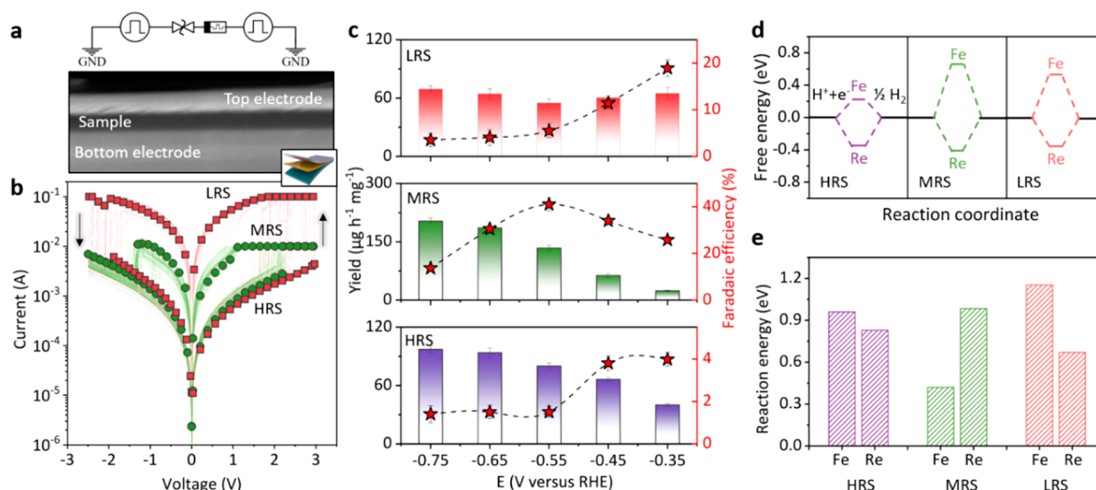


Figure 3. (a) Schematic sketch of the circuit connection (top) and SEM cross-sectional image (bottom). (b) DC switching curves of the FeReS_3 nanosheets. The green and red symbols are the typical current–voltage curves of the FeReS_3 nanosheets at I_{CC} values of 10 mA and 100 mA, respectively. (c) Ammonia yields and Faradaic efficiencies versus different states. (d) Hydrogen adsorption free energy (ΔG_{H}) of FeReS_3 at different resistance states. (e) Reaction energy at the rate-limiting step for FeReS_3 at different resistance states.

PRE axons.^{32,33} Once a PRE spike is emitted, the action potential can be conveyed via its axon to the synapse. Every synaptic response is dependent on the action potential, which is transmitted to the POST from the PRE. The biological synapse, in which the accumulation of a neurotransmitter dictates the synaptic response, can be imitated through a phase change memory (PCM) device (Figure 1b), where the electroconductibility in a dielectric region between two contact electrodes can be regulated by the structural transition. Figure 1c displays the typical properties of a PCM synapse. After the application of a positive voltage, the switching of the synapse, named a set process, between a low-resistance state (LRS) and a high-resistance state (HRS) will take place. The built-in polarization field induced by injecting superfluous carriers transforms the structure into another phase (as shown in Figure 1b). For a negative voltage, the reverse-polarization-driven recovery of the structural transition leads to reversed behavior, called changing-over to HRS from LRS. It is important to note that the conductance in LRS is strongly dependent on the obtained phase structure, which can be controlled by setting the compliance current I_{CC} to trigger a phase transition. With an increasing I_{CC} , more carriers are constrained to participate in the structural transition, thus resulting in another LRS phase that requires more energy. Figure 1d illustrates a physical mechanism of the structural transition and potential application in the NRR. The obvious changes in conductance adequately illustrate that the character of the material has been reimagined, which provides a possibility for discovering extraordinary NRR performance that cannot be observed under conventional conditions. More importantly, this intriguing behavior can be accurately controlled and remembered by recording the I_{CC} value. If the catalytic activity becomes fatigued, the catalysts can be recharged repeatedly to return to the initial state according to our requirements.

RESULTS AND DISCUSSION

When materializing this proposal, it is a good option to produce a double-faced Janus two-dimensional (2D) material with multiple phase transitions under appropriate electrical stimulation. On the basis of our previous work,³⁴ we designed

a new type of Janus FeReS_3 nanostructure using a citric-assisted hydrothermal procedure. The scanning electron microscopy (SEM) result in the upper panel of Figure 2a shows that the FeReS_3 nanosheets are symmetrically distributed to construct a porous morphology. The atomic force microscopy (AFM) result in the lower panel of Figure 2a and the transmission electron microscopy (TEM) (Figure S1) result show that the flower-like nanosheets are 2.3 nm thick and 0.2 μm wide. The X-ray diffraction (XRD) pattern clearly shows the successful formation of the Janus FeReS_3 material (Figure 2b, see the side view in the inset), in which the slight difference between the experimental results and theoretical simulations can be interpreted as changing the geometrical structure factor.³⁵ More importantly, the high-resolution TEM (HR-TEM) and stimulated and experimental selected area electron diffraction (SAED) images in Figure 2c reveal that the designed FeReS_3 possesses the typical features of 2D-layered materials. Janus FeReS_3 with a distinguishable interlayer spacing of ~ 3.0 Å and a single-layer thickness of 6.5 Å can be clearly observed, which highly agrees with the theoretical simulation. In Figures S2 and S3, the energy-dispersive X-ray spectroscopy (EDS) spectra and elemental mappings show the uniform distribution of S, Fe, and Re, and the relative elemental ratio is 3:1:1.

The I_{CC} -dependent in situ Raman measurements show structural transitions of the amplitude modes in different phases (Figure S4a). To compare the peak position and relative intensity among different phases, we transform the obtained spectra I to $(I - I_0)/I_0$, where I_0 is the Raman intensity of the E_{2g} mode at 250 cm^{-1} . The normalized I_{CC} -dependent Raman scattering intensity maps obtained for different phases are shown in Figure 2d. For the initial state, we clearly identify a strong E_{2g} mode at 250 cm^{-1} (middle panel), which can be interpreted as the reverse vibration of the Fe atoms in terms of the S atoms parallel to the Janus FeReS_3 plane (Figure S4b). When $I_{CC} = 10$ mA is applied to this system, the E_{2g} -like mode remains unchanged, but its half-width is enlarged (bottom panel), indicating that symmetry breaking induced by a structural transition weakens phonon confinement (Figure S4c). Upon further increasing the I_{CC} to 100 mA (top panel), an additional Raman mode at 430 cm^{-1}

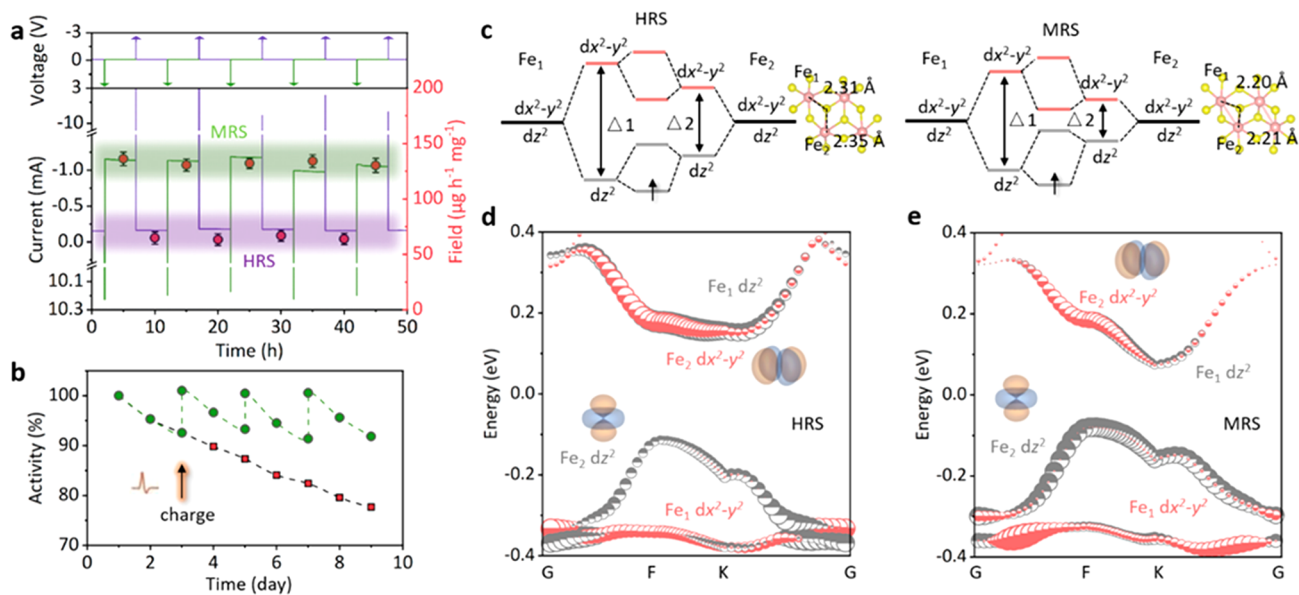


Figure 4. (a) Input waveform (top) and the corresponding sample current state (line) and ammonia yields (symbol). (b) Time-dependent NH_3 yield activity. The green symbol shows the activity of the sample with pulse stimulation every 3 days. (c) Evolution of the electronic states under electrical stimulation. The orbital-resolved band structures of the (d) HRS and (e) MRS.

originating from the A_{1g} mode becomes Raman active. This distinguishable Raman fingerprint, which is sensitive to structural changes, successfully proves the phase transformation when electrical stimulation is applied.

Figure 2e displays the polarization dependence of Raman behavior measured at different resistance states (the corresponding atomic configuration shown in the upper region of Figure 2f), which can more clearly show the structural transition. The isotropic pattern obtained for the E_{2g} mode in the initial state turns into a two-lobe feature at $I_{CC} = 10$ mA, corresponding to a structural transition from an HRS to a middle-resistance state (MRS). Structural analysis reveals that the E_{2g} vibration in the MRS displays a diagonal Raman scattering strength owing to the formation of parallelogram-chained Fe clusters. Conceivably, for an LRS with a triangular configuration, the polarization behavior of the E_{2g} mode exhibits a typical feature of triangular anisotropy. As additional powerful evidence, the resistances of different phases, as an important electrical characteristic, were determined to disclose the differences in their electronic structures. The analysis of the electronic density of states (DOS) and corresponding band structures (Figure S5) disclose that carrier transfer is strongly dependent on electronic occupation at the Fermi energy of the material. The corresponding phase transition potential barriers from the HRS to the LRS and MRS are $\Delta E_1 = 0.13$ eV/atom and $\Delta E_2 = 0.17$ eV/atom. The X-ray photoelectron spectroscopy (XPS) results in Figure S6 and the aforementioned Raman analysis show that an unconventional phase transition occurs in our designed Janus FeReS_3 by using electrical stimulation technology.

The achievement of memristive behavior capable of reserving various phase structures is an essential prerequisite for designing a new type of NRR electrode. To estimate this point, we designed a memristive device comprised of an FeReS_3 active interface, which is accurately located between the top and bottom electrodes (Figure 3a). As a general feature, the FeReS_3 device demonstrates a classic hysteresis response in its current–voltage (I – V) curve at different

voltages (Figure 3b). As a material undergoing structural transition and exhibiting different electronic properties, FeReS_3 shows distinguishable electroforming-free I – V behavior. Along with the existence of a Schottky junction between FeReS_3 and the electrode, the shift among the HRS, MRS and LRS can be triggered by applying a forward bias, such as 1.5–2.2 V for MRS and 1.7–2.9 V for LRS. A reverse bias drives the system back to the HRS, resetting the current at a smaller voltage and displaying a vivid asymmetry in the I – V response. In direct current (DC) operation mode, the overlap among all the current–voltage curves in Figure 3b exhibit nonvolatile and bipolar resistive switching behavior, indicating that the built-in polarization field enables reversible switching of the double-faced FeReS_3 . This memristive behavior in FeReS_3 is generally accompanied by a prominent memcapacitive effect (Figure S7). In addition, the resistance remarkably decreases according to changes in I_{CC} from 10 mA to 100 mA, which is regarded as a multilevel phase structure. Under a reverse bias, the current (I_R) in the off state can be expressed by the equation: $I_R = SA T^2 e^{-q\Phi_B'/kT}$, where S , A^* , k , Φ_B' , and T stand for the contact area, the effectiveness of the Richardson constant, the Boltzmann constant, the apparent Schottky barrier, and the temperature, respectively. In our measurement, the contact areas between FeReS_3 and metal electrodes remain unchanged, suggesting that the contact-potential barrier is responsible for different I_R values. It has been confirmed by the Raman spectra in Figure 2d, e that the structural transition can be triggered by electrical stimulation, in which the work function (WF) potential of FeReS_3 decreases from 4.91 (LRS) to 4.85 eV (MRS) and 4.77 eV (HRS) (Figure S8). Therefore, the low WF difference (Φ_B') that occurs in the LRS results in an obvious enhancement in I_R .

Subsequently, the electrocatalytic performance of FeReS_3 with different phases was determined and shown in Figure 3c for comparison. Noticeably, the catalyst mass remains unchanged except for the phase transition to ensure the fairness of comparison. After an hour of electrocatalysis, the test results show that the Faradaic efficiency (FE) and NH_3

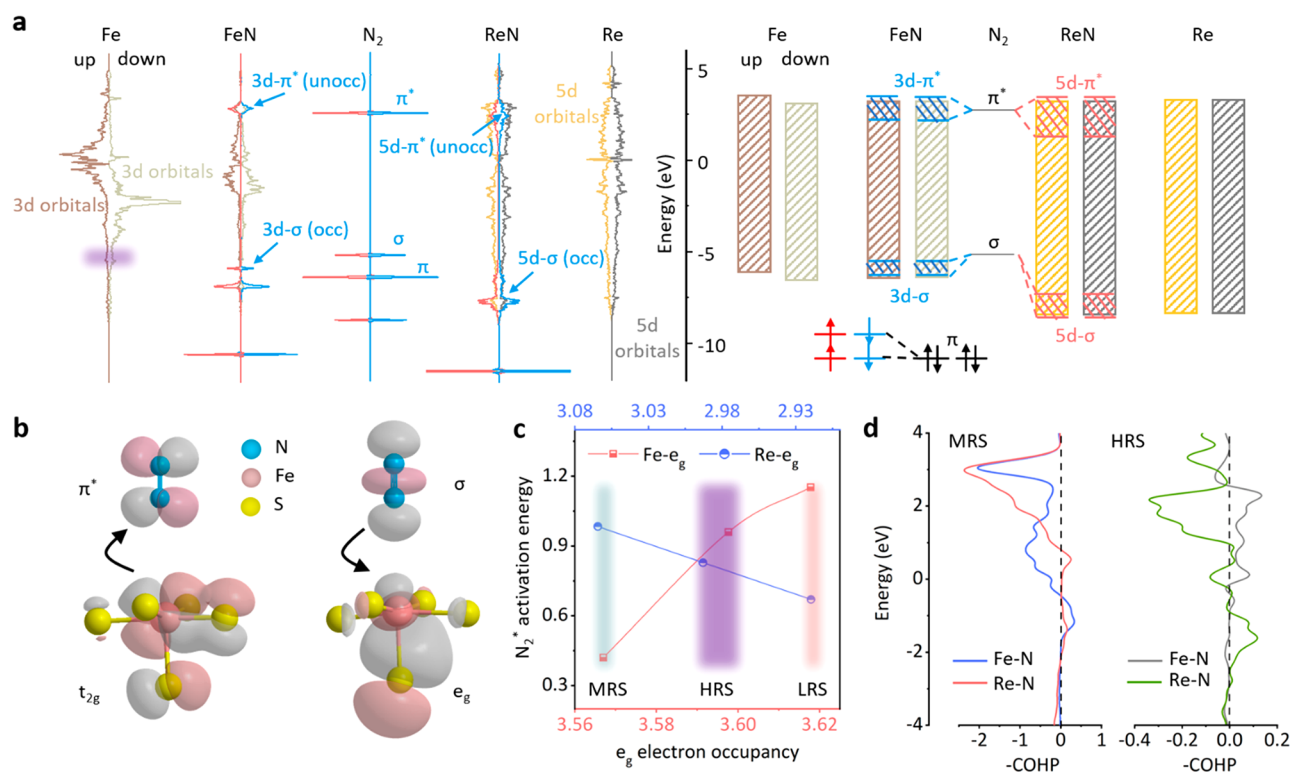


Figure 5. (a) Projected electronic DOS and their interaction between N₂ molecules and reactive sites. (b) N₂ π* orbital receives electrons from the occupied t_{2g} orbital (left). Simultaneously, the N₂ δ orbital provides some electrons to the empty e_g orbital (right). (c) Correlation between FeReS₃ e_g occupation and the catalytic activity for N₂ molecules. (d) COHP analysis of the Fe–N and Re–N bonding interactions in FeReS₃ at different resistance states.

yield rate values in the MRS are obviously better than those in the LRS and HRS. This conclusion can be quantified by colorimetric assays (Nessler's reagent) and 1H NMR spectra (Figures S9–13); notably, the Nafion membrane does not exhibit any ammonia emergence (Figure S14). Regarding the HRS sample, the NH₃ yield increases with an increasing applied voltage. However, the FE value decreases, which can be attributed to the accelerated HER where the protons prefer to dominate the active site and decrease N₂ adsorption. In contrast to the HRS, the increased FE value but decreased NH₃ yield in the LRS sample imply that the NRR catalytic activity cannot be truly improved. Note that the NH₃ yield rate in the MRS is significantly enhanced compared to that in the LRS and HRS, and the maximum FE of 43% occurs at –0.55 eV (Figure S10). This result can be attributed only to the phase-transition-induced enhancement in catalytic activity, leading to a conversion of the pathway reaction. Regarding potential applications, the highest FE and NH₃ yield rates of the FeReS₃ electrode in the MRS are comparable to those reported in current literature (Table S1). The morphology and crystal structure of the FeReS₃ nanosheets remain unchanged after long-term reactions (Figures S15 and 16), indicating good catalytic stability. It is notable that the high selectivity for the NRR in the MRS can also be proven since there is no detectable hydrazine in the product solutions (Figures S17–S19). This result is because the selectivity of the NRR is strongly related to the breakdown of structural symmetry (Figure S20).

To disclose the intrinsic catalytic mechanism, we conducted density functional theory (DFT) to evaluate the HER and NRR activity at the Re and Fe sites, as shown in Figure 3d.

With a structural transition from the HRS to the MRS, the hydrogen adsorption free energy (ΔG_{H}) clearly increases, thereby suppressing the HER. In contrast, compared to that in the LRS and HRS in Figure 3e, the activation energy of the NRR in the MRS is significantly reduced, and site conversion is activated from the Re site to the Fe site (detailed reaction pathway shown in Figure S20). This analysis of the HER and NRR activity can be used to intuitively explain the improvement in NRR performance.

To confirm the memristive characteristic of catalytic activity, the phase conversion-dependent NH₃ yield rate is shown in Figure 4a. When electrical pulses at positive 3 V are input, the FeReS₃ system cannot keep an increased current value but sharply recovers to its MRS (marked by green shades) and demonstrates long-term steady operation for 5 h. After applying negative electrical stimulation, an abrupt jump from the MRS to the HRS (marked by purple shades) occurs, demonstrating controllable switching dynamics (Figure S21). Notably, the average NH₃ yield can fluctuate during the reversible phase transition, which indicates that catalytic activity can be regulated and remembered repeatedly. Catalytic performance fatigue in phase-related catalysts is another critical factor that needs to be considered, especially for phases with high catalytic activity. The time-dependent NH₃ yield in Figure 4b shows that the yield slowly decreases by approximately 20% in 192 h (8 days) (red squares) because the MRS phase sluggishly converts back into the more stable HRS phase. In this process, the catalyst is clearly distinguishable from conventional unstable catalysts with irreversible structural damage. The catalytic activity can be easily resumed using a simple recharging operation due to the memristive character-

istics (green circles) of the catalyst. This outstanding catalytic performance and particular memristive characteristics show high promise for use in NRR applications.

According to the octahedral ligand field, the structural transition induced by electric stimulation can be explained by the detailed orbital analysis in Figure 4c. Regarding the electronic structure of the HRS (Figure 4d), the asymmetric Fe–S units make the 3d orbital split into higher Fe₁ d_{x²-y² and lower Fe₂ d_{z²} orbitals in the valence bands, whereas a flat conduction band is composed of Fe₂ d_{x²-y² and Fe₁ d_{z²} orbitals, creating a 0.272 eV band gap. Most electrons prefer to occupy the bonding state (marked by black arrows) formed by d_{z²} orbital hybridization, but this nonequivalent electron occupation makes the Fe₁–S bond length (2.31 Å) and Fe₂–S bond length (2.35 Å) different. When superfluous carriers induced by electrical stimulation are intentionally implanted to reconstruct the antibonding state of Fe₂ d_{x²-y² and Fe₁ d_{z²} orbitals, the difference between the Fe₁–S and Fe₂–S decreases, resulting in a smaller band gap and a parabolic conduction band (Figure 4e). Thus, the hybridization between Fe₁–S and Fe₂–S is enforced to generate the MRS structure, and the remaining electrons will hybridize with each other to form additional symmetric metallic bonds (pink bond between Fe₁ and Fe₂), as shown in the right panel of Figure 4c. The orbital-resolved bands in Figure 4d show that the energy splitting between the d_{x²-y² and d_{z²} orbitals in the HRS ($\Delta 1$ and $\Delta 2$) is much larger than that of the MRS in Figure 4e, which demonstrates the orbital hybridization priority in the MRS with electrical stimulation (right panel of Figure 4c). In addition, the decreased band gap in the MRS endows the system with an excellent low-resistance feature, which is advantageous for regulating NRR performance (Figure S22).}}}}

To elaborate the bonding features, we compare the orbital-resolved DOS of N₂ activation at the Fe and Re sites of the MRS in Figure 5a. In the conduction band region, the spin-down energy levels of the Fe 3d orbitals and N₂ π^* orbitals are coordinated well with each other, creating the appearance of unoccupied 3d- π^* . Strong 3d orbital localization provides a large exchange stabilization energy at the valence band tail (marked by purple shadow), which has obvious advantages for promoting charge transfer from the N₂ δ orbital to the partially occupied Fe 3d orbital. After orbital hybridization, the 3d- δ bonding state is approximately 0.66 eV smaller than that of N- δ orbitals, thus forcing *N_2 to be absorbed and activated. Regarding the Re site, the electronic states of the 5d orbital becomes delocalized, which weakens the interaction between *N_2 and the Re site. If the electron occupied at the N₂ δ orbital is transferred to the unoccupied 5d orbital to form a 5d- δ bonding state, more energy needs to be provided, leading to a higher N–N bond order. Therefore, a higher dissociation barrier occurs at the Re site instead of the Fe site. Regarding the N₂ molecule, a lone-pair δ orbital can donate electrons to the e_g orbital reaction site, whereas the N₂ π^* orbital receives electrons from the t_{2g} orbitals (Figure 5b).

Generally, the catalytic interaction between N₂ and the reaction site can be reflected by the process of the “acceptance-donation” of electrons, where controlling the unfilled and occupied d orbitals of the active site plays a determining role in accelerating the NRR.³⁶ N₂ molecules prefer a tilted configuration, allowing their π^* orbital to overlap with the e_g orbital of the metal site. As a result, e_g occupancy discloses the strength of the bond between the adsorbate and catalyst surface (Figure 5c). As a structural transition from the HRS to

the MRS, the decreased e_g occupancy at the Fe site leads to a decreased adsorption energy, while the Re site demonstrates the opposite behavior, resulting in the conversion of active sites.

To compare the bonding characteristics of Fe–N and Re–N, we calculated the crystal orbital Hamilton population (COHP) in Figure 5d. Compared with the Fe–N bonding contribution for the HRS, an obvious antibonding state from the Re–N bond appears at the Fermi level, indicating that the electrons from the Re 5d orbital are partially donated to the unfilled π^* orbital. The stability of the Re–N bond is lower than that of the Fe–N bond, thus forcing *N_2 to be active at the Re site for subsequent hydrogenation. Regarding the MRS, Fe–N bonds transform into an antibonding state from a bonding state at the Fermi level; thus, the adsorbed *N_2 on the Fe site can be activated more easily. These detailed orbital analyses confirm that the active site conversion induced by structural transition plays a vital role in enhancing NRR performance.

CONCLUSION

In this work, we have demonstrated that electrical stimulation can lead to an intriguing structural transition to boost NRR performance, and this method is inspired by the learning networks of spiking neurons. Notably, the optimized catalytic activity can be remembered and recovered repeatedly through a simple charging operation. Our findings offer new insight for boosting NRR performance in electrocatalysis, photocatalysis and photoelectrochemical catalysis. Because of the variety of candidate materials, it is feasible for this strategy to be widely adopted to optimize catalytic performance.

EXPERIMENTAL SECTION

Preparation of the Ultrathin FeReS₃ Nanosheets. During the synthesis procedure, 100 mg of iron acetylacetonate was suspended in 10 mL of deionized water with vigorous stirring. With ultrahigh purity argon (Ar, 99.999%) protection, 10 mL of aqueous solution including 18.5 mM sodium perrhenate and 0.65 M thiourea were injected into a Pyrex reactor. The rate of the syringe pump was controlled at 2 mL min⁻¹. The solution was refluxed at 278 K for approximately 1 h while stirring to ensure that the solution dispersed adequately. To obtain qualified ultrathin FeReS₃ nanosheets, a sodium citrate aqueous solution (2 mL, 0.1 wt %) was steadily added dropwise with Ar protection before the hydrothermal process. The solution was sealed in a Teflon-lined stainless steel autoclave (25 mL) for 15 h at 523 K. The supernatant was removed when the autoclave cooled to room temperature. The black precipitates were rinsed thoroughly with absolute ethanol and deionized water and freeze-dried under vacuum. The crystallization and purity of FeReS₃ was improved using an annealing procedure. Ceramic boats were inserted together with the nanosheets into a horizontal quart tubular reactor. The reactor was cleaned with 500 sccm Ar for 2 h before the heating process began. The furnace was maintained at 537 K for 1 h with a 150 sccm Ar flow, which helped prevent oxidation. The pressure under the whole annealing process was reduced to less than 1×10^{-2} Torr.

Electrochemical NRR Measurements. The electrochemical (EC) measurements were conducted with a CHI 660D electrochemical workstation at room temperature using a N₂-saturated 0.5 M K₂SO₄ solution. The two independent compartment cells were connected with a Celgard 3401 membrane. Before the NRR test, the Celgard membrane was sequentially heated in boiling water, H₂O₂ 5% aqueous solution, dilute H₂SO₄ (0.5 M) and ultrapure water for 120 min, respectively. A graphite rod (Alfa Aesar, 99.9995%), modified glassy carbon electrode, and saturated Ag/AgCl electrode were utilized as the counter, working and reference electrodes, respectively. Stable polarization curves could be achieved after several cycles. The

working electrodes were prepared as follows. First, 8 mg of the sample was blended with 5 wt % Nafion (0.3 mL), ethanol (0.7 mL), and ultrapure water (2 mL). The mixed solution was sonicated for 1 h until a homogeneous ink was observed. Subsequently, the catalyst ink (6 μL) was dropwise applied on the working electrode (φ , 3 mm). The residual air in the reaction system was removed before electrolysis by constantly blowing ultrahigh purity nitrogen (N_2) for 0.5 h. Then, N_2 was continuously injected into the cathodic compartment with constant stirring during the EC reaction. After the NRR, the cathodic electrolyte was collected and quantified by a chromogenic reaction.

DFT Calculation Details. The Gibbs free energies on the catalyst surface for all H_2 and N_2 reduction reactions were calculated by the Vienna ab initio simulation package (VASP),^{14,37,38} which is based on the Perdew–Burke–Ernzerhof functions and generalized gradient approximation.^{39,40} The Monkhorst–Pack k -point was set to $9 \times 9 \times 1$. The plane-wave energy cutoff was set to 480 eV. All forces on the free ions were 0.01 eV/Å, which were adopted to relax the surface slab with an 18 Å vacuum space.

■ ASSOCIATED CONTENT

■ Supporting Information

The Supporting Information is available free of charge at <https://pubs.acs.org/doi/10.1021/jacs.0c12458>.

Experimental details, more characterization results during sample preparation and evaluation, and detailed discussions of kinetics results (PDF)

■ AUTHOR INFORMATION

Corresponding Authors

Peifang Wang – Key Laboratory of Integrated Regulation and Resource Development on Shallow Lake of Ministry of Education, College of Environment, Hohai University, Nanjing 210098, P. R. China; orcid.org/0000-0003-3010-1008; Email: pfwang2005@hhu.edu.cn

Lizhe Liu – Institute of Collaborative Innovation Center of Advanced Microstructures, National Laboratory of Solid State Microstructures, Nanjing University, Nanjing 210093, P. R. China; orcid.org/0000-0001-5111-0750; Email: lzliu@nju.edu.cn

Yan Sun – Department of Chemistry, University of Utah, Salt Lake City, Utah 84112, United States; orcid.org/0000-0001-7001-7834; Email: elaine.sun@utah.edu

Authors

Gang Zhou – Key Laboratory of Integrated Regulation and Resource Development on Shallow Lake of Ministry of Education, College of Environment, Hohai University, Nanjing 210098, P. R. China

Tinghui Li – College of Electronic Engineering, Guangxi Normal University, Guilin 541004, P. R. China

Rong Huang – Key Laboratory of Integrated Regulation and Resource Development on Shallow Lake of Ministry of Education, College of Environment, Hohai University, Nanjing 210098, P. R. China

Bin Hu – Key Laboratory of Integrated Regulation and Resource Development on Shallow Lake of Ministry of Education, College of Environment, Hohai University, Nanjing 210098, P. R. China

Hao Li – Key Laboratory of Integrated Regulation and Resource Development on Shallow Lake of Ministry of Education, College of Environment, Hohai University, Nanjing 210098, P. R. China

Complete contact information is available at:

<https://pubs.acs.org/10.1021/jacs.0c12458>

Funding

Natural Science Foundation of Jiangsu Province (SBK2020043594) Fundamental Research Funds for the Central Universities (B200201014, B200204033, 0204–14380083), PAPD Major Science and Technology Program for Water Pollution Control and Treatment (2017ZX07204003), Key Program of National Natural Science Foundation of China (92047201, 91647206), National Basic Research Programs of China (2018YFA0306004), National Science Funds for Creative Research Groups of China (51421006), and National Natural Science Foundation (61964004).

Notes

The authors declare no competing financial interest.

■ REFERENCES

- (1) van der Ham, C. J. M.; Koper, M. T. M.; Hetterscheid, D. G. H. Challenges in reduction of dinitrogen by proton and electron transfer. *Chem. Soc. Rev.* **2014**, *43*, 5183.
- (2) Guo, C. X.; Ran, J. R.; Vasileff, A.; Qiao, S. Z. Rational design of electrocatalysts and photo(electro)catalysts for nitrogen reduction to ammonia (NH_3) under ambient conditions. *Energy Environ. Sci.* **2018**, *11*, 45.
- (3) Deng, J.; Iniguez, J. A.; Liu, C. Electrocatalytic nitrogen reduction at low temperature. *Joule* **2018**, *2*, 846.
- (4) Cao, N.; Zheng, G. F. Aqueous electrocatalytic N_2 reduction under ambient conditions. *Nano Res.* **2018**, *11*, 2992.
- (5) Ertl, G. Reactions at surfaces: From atoms to complexity. *Angew. Chem., Int. Ed.* **2008**, *47*, 3524.
- (6) Guo, X. Y.; Gu, J. X.; Lin, S. R.; Zhang, S. L.; Chen, Z. F.; Huang, S. P. Tackling the activity and selectivity challenges of electrocatalysts toward the nitrogen reduction reaction via atomically dispersed Biatom catalysts. *J. Am. Chem. Soc.* **2020**, *142*, 5709.
- (7) Li, S. J.; Bao, D.; Shi, M. M.; Wulan, B. R.; Yan, J. M.; Jiang, Q. Amorphizing of Au nanoparticles by CeO_x -RGO hybrid support towards highly efficient electrocatalyst for N_2 reduction under ambient conditions. *Adv. Mater.* **2017**, *29*, 1700001.
- (8) Wu, X. L.; Xiong, S. J.; Liu, Z.; Chen, J.; Shen, J. C.; Li, T. H. P.; Wu, H.; Chu, P. K. Green light stimulates terahertz emission from mesocrystal microspheres. *Nat. Nanotechnol.* **2011**, *6*, 103.
- (9) Wu, T. W.; Zhu, X. J.; Xing, Z.; Mou, S. Y.; Li, C. B.; Qiao, Y. X.; Liu, Q.; Luo, Y. L.; Shi, X. F.; Zhang, Y. N.; Sun, X. P. Greatly improving electrochemical N_2 Reduction over TiO_2 nanoparticles by iron doping. *Angew. Chem., Int. Ed.* **2019**, *58*, 18449.
- (10) Xue, Z. H.; Zhang, S. N.; Lin, Y. X.; Su, H.; Zhai, G.-Y.; Han, J. T.; Yu, Q. Y.; Li, X. H.; Antonietti, M.; Chen, J. S. Electrochemical reduction of N_2 into NH_3 by donor–acceptor couples of Ni and Au nanoparticles with a 67.8% Faradaic efficiency. *J. Am. Chem. Soc.* **2019**, *141*, 14976.
- (11) Hao, Y. C.; Guo, Y.; Chen, L. W.; Shu, M.; Wang, X. Y.; Bu, T. A.; Gao, W. Y.; Zhang, N.; Su, X.; Feng, X.; et al. Promoting nitrogen electroreduction to ammonia with bismuth nanocrystals and potassium cations in water. *Nat. Catal.* **2019**, *5*, 448.
- (12) Kobayashi, D.; Kobayashi, H.; Wu, D. S.; Okazoe, S.; Kusada, K.; Yamamoto, T.; Toriyama, T.; Matsumura, S.; Kawaguchi, S.; Kubota, Y.; Aspera, S. M.; Nakanishi, H.; Arai, S.; Kitagawa, H. Significant enhancement of hydrogen evolution reaction activity by negatively charged Pt through light doping of W. *J. Am. Chem. Soc.* **2020**, *142*, 17250.
- (13) Montoya, J. H.; Tsai, C.; Vojvodic, A.; Nørskov, J. K. The challenge of electrochemical ammonia synthesis: A new perspective on the role of nitrogen scaling relations. *ChemSusChem* **2015**, *8*, 2180.
- (14) Fu, Y.; Li, T. H.; Zhou, G.; Guo, J. H.; Ao, Y. H.; Hu, Y. Y.; Shen, J. C.; Liu, L. Z.; Wu, X. L. Dual-metal-driven selective pathway

of nitrogen reduction in orderly atomic-hybridized Re_2MnS_6 ultrathin nanosheets. *Nano Lett.* **2020**, *20*, 4960.

(15) Wang, X.; Zhang, Y. W.; Si, H. N.; Zhang, Q. H.; Wu, J.; Gao, L.; Wei, X. F.; Sun, Y.; Liao, Q. L.; Zhang, Z.; Ammarah, K.; Gu, Lin; Kang, Z.; Zhang, Y. Single-atom vacancy defect to trigger high-efficiency hydrogen evolution of MoS_2 . *J. Am. Chem. Soc.* **2020**, *142*, 4298.

(16) Fajardo, J.; Peters, J. C. Catalytic nitrogen-to-ammonia conversion by osmium and ruthenium complexes. *J. Am. Chem. Soc.* **2017**, *139*, 16105.

(17) Yao, Y.; Zhu, S. Q.; Wang, H. J.; Li, H.; Shao, M. H. A spectroscopic study on the nitrogen electrochemical reduction reaction on gold and platinum surfaces. *J. Am. Chem. Soc.* **2018**, *140*, 1496.

(18) Lv, C. D.; Yan, C. S.; Chen, G.; Ding, Y.; Sun, J. X.; Zhou, Y. S.; Yu, G. H. An amorphous noble-metal-free electrocatalyst that enables nitrogen fixation under ambient conditions. *Angew. Chem., Int. Ed.* **2018**, *57*, 6073.

(19) Bao, D.; Zhang, Q.; Meng, F. L.; Zhong, H. X.; Shi, M. M.; Zhang, Y.; Yan, J. M.; Jiang, Q.; Zhang, X. B. Electrochemical reduction of N_2 under ambient conditions for artificial N_2 fixation and renewable energy storage using N_2/NH_3 cycle. *Adv. Mater.* **2017**, *29*, 604799.

(20) Chen, G. F.; Cao, X. R.; Wu, S. Q.; Zeng, X. Y.; Ding, L. X.; Zhu, M.; Wang, H. H. Ammonia electrosynthesis with high selectivity under ambient conditions via a Li^+ incorporation strategy. *J. Am. Chem. Soc.* **2017**, *139*, 9771.

(21) Zhao, J. X.; Chen, Z. F. Single Mo atom supported on defective boron nitride monolayer as an efficient electrocatalyst for nitrogen fixation: A computational study. *J. Am. Chem. Soc.* **2017**, *139*, 12480.

(22) Liu, C. W.; Li, Q. Y.; Wu, C. Z.; Zhang, J.; Jin, Y. G.; MacFarlane, D. R.; Sun, C. H. Single-boron catalysts for nitrogen reduction reaction. *J. Am. Chem. Soc.* **2019**, *141*, 2884.

(23) Wang, D. B.; Azofra, L. M.; Harb, M.; Cavallo, L.; Zhang, X. Y.; Suryanto, B. H. R.; MacFarlane, D. R. Energy-efficient nitrogen reduction to ammonia at low overpotential in aqueous electrolyte under ambient conditions. *ChemSusChem* **2018**, *11*, 3416.

(24) Liu, Y. W.; Cheng, M.; He, Z. H.; Gu, B. C.; Xiao, C.; Zhou, T. F.; Guo, Z. P.; Liu, J. D.; He, H. Y.; Ye, B. J.; Pan, B. C.; Xie, Y. Pothole-rich ultrathin WO_3 nanosheets that trigger N equivalent to N Bond activation of nitrogen for direct nitrate photosynthesis. *Angew. Chem., Int. Ed.* **2019**, *58*, 731.

(25) Han, L. L.; Liu, X. J.; Chen, J. P.; Lin, R. Q.; Liu, H. X.; Lu, F.; Bak, S.; Liang, Z. X.; Zhao, S. Z.; Stavitski, E.; Luo, J.; Adzic, R. R.; Xin, H. L. L. Atomically dispersed molybdenum catalysts for efficient ambient nitrogen fixation. *Angew. Chem., Int. Ed.* **2019**, *58*, 2321.

(26) Shi, Y.; Liang, X.; Yuan, B.; Chen, V.; Li, H.; Hui, F.; Yu, Z.; Yuan, F.; Pop, E.; Wong, H.-S. P.; Lanza, M. Electronic synapses made of layered two-dimensional materials. *Nat. Electron.* **2018**, *1*, 458.

(27) Wei, W.; Pedretti, G.; Milo, V.; Carboni, R.; Calderoni, A.; Ramaswamy, N.; Spinelli, A. S.; Ielmini, D. Learning of spatiotemporal patterns in a spiking neural network with resistive switching synapses. *Sci. Adv.* **2018**, *4*, 4752.

(28) Ohno, T.; Hasegawa, T.; Tsuruoka, T.; Terabe, K.; Gimzewski, J. K.; Aono, M. Short-term plasticity and long-term potentiation mimicked in single inorganic synapses. *Nat. Mater.* **2011**, *10*, 591.

(29) van de Burgt, Y.; Lubberman, E.; Fuller, E. J.; Keene, S. T.; Faria, G. C.; Agarwal, S.; Marinella, M. J.; Alec Talin, A.; Salleo, A. A non-volatile organic electrochemical device as a low-voltage artificial synapse for neuromorphic computing. *Nat. Mater.* **2017**, *16*, 414.

(30) Zhu, X. J.; Li, D.; Liang, X. G.; Lu, W. D. Ionic modulation and ionic coupling effects in MoS_2 devices for neuromorphic computing. *Nat. Mater.* **2019**, *18*, 141.

(31) Zhang, F.; Zhang, H. R.; Krylyuk, S.; Milligan, C. A.; Zhu, Y. Q.; Zemlyanov, D. Y.; Bendersky, L. A.; Burton, B. P.; Davydov, A. V.; Appenzeller, J. Electric-field induced structural transition in vertical MoTe_2 - and $\text{Mo}_{1-x}\text{W}_x\text{Te}_2$ -based resistive memories. *Nat. Mater.* **2019**, *18*, 55.

(32) Yang, J. J.; Strukov, D. B.; Stewart, D. R. Memristive devices for computing. *Nat. Nanotechnol.* **2013**, *8*, 13.

(33) Ielmini, D. Resistive switching memories based on metal oxides: Mechanisms, reliability and scaling. *Semicond. Sci. Technol.* **2016**, *31*, 063002.

(34) Fu, Y.; Shan, Y.; Zhou, G.; Long, L. Y.; Wang, L. L.; Yin, K. B.; Guo, J. H.; Shen, J. C.; Liu, L. Z.; Wu, X. L. Electric strain in dual metal Janus nanosheets induces structural phase transition for efficient hydrogen evolution. *Joule* **2019**, *3*, 2955.

(35) Liu, Z.; Wen, X. D.; Wu, X. L.; Gao, Y. J.; Chen, H. T.; Zhu, J.; Chu, P. K. Intrinsic dipole-field-driven mesoscale crystallization of core-shell ZnO mesocrystal microspheres. *J. Am. Chem. Soc.* **2009**, *131*, 9405.

(36) Légaré, M. A.; Belanger-Chabot, G.; Dewhurst, R. D.; Welz, E.; Krummenacher, I.; Engels, B.; Braunschweig, H. Nitrogen fixation and reduction at boron. *Science* **2018**, *359*, 896.

(37) Zhou, G.; Shan, Y.; Wang, L. L.; Hu, Y. Y.; Guo, J. H.; Hu, F. R.; Shen, J. C.; Gu, Y.; Cui, J. T.; Liu, L. Z.; Wu, X. L. Photoinduced semiconductor-metal transition in ultrathin troilite FeS nanosheets to trigger efficient hydrogen evolution. *Nat. Commun.* **2019**, *10*, 399.

(38) Zhou, G.; Shan, Y.; Hu, Y. Y.; Xu, X. Y.; Long, L. Y.; Zhang, J. L.; Dai, J.; Guo, J. H.; Shen, J. C.; Li, S.; Liu, L. Z.; Wu, X. L. Half-metallic carbon nitride nanosheets with micro grid mode resonance structure for efficient photocatalytic hydrogen evolution. *Nat. Commun.* **2018**, *9*, 3366.

(39) Li, L.; Tuo, W.; Zhu, Q. H.; Sepehrpour, H.; Yao, Y.; Yan, C. G.; Liu, L. Z.; Li, D.; Xie, Y. J.; Zhang, C.; Wang, M.; Sun, Y. Resorcinarene induced assembly of carotene and lutein into hierarchical superstructures. *J. Am. Chem. Soc.* **2020**, *142*, 20583.

(40) Sun, Y.; Chen, C. Y.; Liu, J. B.; Liu, L. Z.; Tuo, W.; Zhu, H. T. Z.; Lu, S.; Li, X. P.; Stang, P. J. Self-assembly of porphyrin-based metallacages into octahedra. *J. Am. Chem. Soc.* **2020**, *142*, 17903.